

PAPER • OPEN ACCESS

Femtosecond laser fabrication of nanograting-based distributed fiber sensors for extreme environmental applications

To cite this article: Mohan Wang *et al* 2021 *Int. J. Extrem. Manuf.* **3** 025401

View the [article online](#) for updates and enhancements.

Femtosecond laser fabrication of nanograting-based distributed fiber sensors for extreme environmental applications

Mohan Wang¹ , Kehao Zhao¹, Jingyu Wu¹, Yuqi Li¹, Yang Yang^{1,2} , Sheng Huang¹ , Jieru Zhao¹, Thomas Tweedle³, David Carpenter⁴, Guiqiu Zheng⁴ , Qingxu Yu²  and Kevin P Chen¹ 

¹ Department of Electrical and Computer Engineering, University of Pittsburgh, Pittsburgh, PA 15261, United States of America

² School of Optoelectronic Engineering and Instrument Science, Dalian University of Technology, Dalian 116081, People's Republic of China

³ Westinghouse Electric Company LLC, Pittsburgh, PA 15235, United States of America

⁴ Nuclear Reactor Laboratory, Massachusetts Institute of Technology, 138 Albany Street, Cambridge, MA 02139, United States of America

E-mail: pec9@pitt.edu

Received 23 September 2020, revised 5 December 2020

Accepted for publication 28 January 2021

Published 16 February 2021



Abstract

The femtosecond laser has emerged as a powerful tool for micro- and nanoscale device fabrication. Through nonlinear ionization processes, nanometer-sized material modifications can be inscribed in transparent materials for device fabrication. This paper describes femtosecond precision inscription of nanograting in silica fiber cores to form both distributed and point fiber sensors for sensing applications in extreme environmental conditions. Through the use of scanning electron microscope imaging and laser processing optimization, high-temperature stable, Type II femtosecond laser modifications were continuously inscribed, point by point, with only an insertion loss at 1 dB m⁻¹ or 0.001 dB per point sensor device. High-temperature performance of fiber sensors was tested at 1000 °C, which showed a temperature fluctuation of ±5.5 °C over 5 days. The low laser-induced insertion loss in optical fibers enabled the fabrication of a 1.4 m, radiation-resilient distributed fiber sensor. The in-pile testing of the distributed fiber sensor further showed that fiber sensors can execute stable and distributed temperature measurements in extreme radiation environments. Overall, this paper demonstrates that femtosecond-laser-fabricated fiber sensors are suitable measurement devices for applications in extreme environments.

Keywords: femtosecond laser manufacturing, optical fiber sensor, device fabrication, extreme environment sensing



Original content from this work may be used under the terms of the [Creative Commons Attribution 3.0 licence](https://creativecommons.org/licenses/by/3.0/).

Any further distribution of this work must maintain attribution to the author(s) and the title of the work, journal citation and DOI.

1. Introduction

Many industrial processes take place under extreme physical conditions. Additive manufacturing systems, advanced propulsion systems, and nuclear and fossil fuel production processes all involve various extreme conditions in their environments, such as high temperatures, strong radiation, and high pressures, among others. A common challenge to optimizing processes that occurs in extreme environments is the lack of tools that can gather high temporal and spatial resolution information. For decades, very few electronic sensors (e.g. thermocouples) were considered suitable for measurements in extreme environmental conditions. Moreover, electronic sensors are point devices, which limit the spatial resolution of measurements. The deployment of electronic sensors in extreme environments also involves significant installation challenges as each sensor must have dedicated wiring and reading instruments.

In addition to electronic sensors, both silica and sapphire optical fibers have demonstrated exceptional stability under harsh environmental conditions [1, 2]. These optical fibers are miniature light-guiding devices that are chemically inert, resilient to radiation and high temperatures, and immune to strong electromagnetic fields. Unmodified optical fibers are able to perform distributed sensing over a long distance with a high spatial resolution by utilizing the intrinsic scattering inside the fiber core. Meanwhile, using advanced laser manufacturing techniques, multiplexable point fiber sensors, such as fiber Bragg gratings (FBGs), can also be fabricated in the optical fiber to perform multipoint measurements using a single fiber. The sensing measurement does not require complicated wiring as both the measurement and signal transmission are possible using the same fiber sensor. With these unique traits, fiber sensors are a promising alternative candidate to address the challenging environmental monitoring requirements in extreme environments.

Fiber optics point sensors based on FBGs are one of the most well-developed optical fiber sensing devices widely used to perform various measurements. Traditionally, FBGs have been fabricated using ultraviolet (UV) lasers with continuous wave (cw) or ns pulse duration outputs [3, 4]. Using various interferometry exposure schemes, such as the phase mask approach, FBGs can be fabricated with very low insertion loss, thus enabling dense multiplexation of many FBGs for high spatial resolution measurements [5, 6]. However, the UV-laser-fabricated FBG requires photosensitized fibers through special dopants in fiber cores or a photosensitization process, such as hydrogen loading. Moreover, the UV-laser-produced FBGs cannot sustain temperatures higher than 300 °C and are erased at a temperature of 700 °C unless further processed [4, 7].

Alternatively, femtosecond lasers, with an output usually at the near infrared (IR) wavelength, have also been used to fabricate fiber sensor devices, such as FBGs. With

their highly localized microscale focus and ultrashort pulse duration, on the order of 10^{-15} s, femtosecond lasers can deposit optical energy with extremely high intensity, up to 10^{14} W cm⁻², at the focal volume to initiate a whole host of nonlinear absorption processes [8, 9]. Through these nonlinear laser-material interactions, femtosecond lasers can be used to inscribe FBGs using interferometry exposure (e.g. bulk interferometer and phase mask), an approach akin to UV laser FBG fabrication [10, 11]. Since the femtosecond laser can produce highly confined material modifications through nonlinear absorption, different direct writing schemes have also been developed. Depending on the writing geometry and procedure, these methods include: point by point [12, 13], plane by plane [14], line by line [15], pitch by pitch [16], and continuous scanning [12].

There are generally three regimes of femtosecond-laser-induced material modification [17, 18]. When the laser pulse intensity is sufficiently high within the focal volume, nonlinear ionization takes place, generating isotropic refractive index changes, also known as Type I modification. This regime is typically used to fabricate both optical devices and three dimensional (3D) photonic circuits inside transparent bulk material [19]. With a higher energy threshold, self-assembled nanostructures with subwavelength periods can be introduced at the laser focal spot, known as nanograting. This regime, or Type II modification, is characterized by its anisotropy, higher loss, and impressive thermal durability [20]. Nanograting has been exploited to fabricate birefringent devices and produce microfluidic channels in femtosecond-laser-assisted etching [21, 22]. A third regime exists wherein the laser intensity continues to increase, resulting in an irreversible optical breakdown. In this regime, microexplosions are introduced inside the material or as ablation on the material surface and can be used for precise micromachining or 3D high-density memory applications [23].

Both the Type I and Type II femtosecond laser modification regimes have been used to fabricate FBGs, which correspond to the Type I-IR and Type II-IR FBG [24]. The Type I modification exhibits low loss and provides a uniform output. Also, the effect is similar to those refractive index changes induced by UV laser irradiation [4]. However, these Type I FBGs often degrade at 1000 °C if not further processed, while the Type II FBGs have demonstrated long-term stability with minimal decay in both high temperature, up to 1000 °C [3, 4, 24–33], and radioactive environments [29]. The exceptionally harsh environmental resistance of Type II FBGs is inseparable from femtosecond-laser-inscribed nanograting, which was found to have exceptional long-term stability under 1100 °C [30, 31]. Moreover, various research studies have also confirmed the formation of nanograting inside the fiber core of Type II FBGs [32, 33].

Though fiber sensors fabricated with the femtosecond laser Type II modification exhibit exceptional high stability under extreme temperatures, they incur higher insertion losses as compared to fiber sensors fabricated by femtosecond Type I modifications or UV laser modifications with cw or ns laser

Table 1. Comparison of the optical fiber sensor insertion loss when using different laser fabrication techniques.

Operating temperature		UV laser type I		FS laser type I		FS laser type II	
		Degrade at >300 °C and erased at 700 °C [4, 7]		Degrade at 1000 °C over long-term [24–33]		Long-term stability at 1000 °C [24–33]	
Insertion loss @ 1550 nm (silica core, single-mode fiber)	FBG	Phase mask	0.002 dB [5]	Phase mask	<0.05 dB [11]	Phase mask	~0.1 dB [25]
				Point by point	~0.65 dB [12]	Point by point	<1 dB [13]
				Plane by plane	<0.02 dB [14]	Plane by plane	~0.8 dB [14]
				Line by line	<0.5 dB [15]		
				Pitch by pitch	~0.3 dB [16]		
				Continuous scan	~0.1 dB [12]		
	IFPI	FBG reflector	0.002 dB [5]	Refractive index dot reflector	0.13 dB [34]	Nanograting reflector	0.002 dB [35]
	Rayleigh enhanced	Continuous scan	0.0015 dB cm ⁻¹ [36]	Continuous scan	0.0008 dB cm ⁻¹ [37]	Continuous scan	0.01 dB cm ⁻¹ [38]

pulses. The high insertion losses incurred in Type II femtosecond modifications could be attributed to light scattering by the nanogratings formed in fiber cores [20]. Table 1 summarizes the out-of-band insertion loss of FBG sensor devices fabricated using both the cw or ns UV and femtosecond lasers, as previously reported in research studies. Even though both the UV-laser- and femtosecond-laser-fabricated FBGs are manufactured from the periodic laser-induced modification, UV-laser-fabricated FBGs can have an insertion loss as low as 0.002 dB [10], while the insertion losses of the femtosecond laser fabricated Type I FBGs are much higher. Prior research studies report insertion losses of Type I FBGs fabricated by femtosecond lasers at <0.1 dB [10–15]; however, these losses are highly dependent on FBG parameters, such as grating strength and fabrication methods. In sharp contrast, the typical insertion losses of the Type II FBG are between 0.1 and 1 dB [13, 14, 25]. The increased insertion loss of the Type II FBG could limit the multiplexing capability of these fiber sensors.

In-fiber Fabry–Perot interferometer (FPI) or intrinsic Fabry–Perot interferometer (IFPI) sensors are promising alternatives to FBGs. The challenge related to the Type II FBGs can be addressed by Type II IFPI sensors. The FBGs are composed of thousands of periodic Type II modifications. For example, a 1 cm long FBG with 50% duty cycles consists of a 5 mm section of fiber core with nanograting structures, whereas an IFPI sensor is composed of only a pair of μm size reflectors inside the optical fiber core. Scattered guided light from the two reflectors is sufficient to produce interference fringes. These fringes can be used to extract the IFPI cavity length changes caused by physical parameter changes. As a result, the insertion loss incurred by nanograting-induced light scattering can be significantly reduced. Overall, this process improves the multiplexability of high-temperature stable fiber sensors. Femtosecond lasers have been used to fabricate Type I IFPIs as temperature, strain, pressure, vibration, and gas concentration sensors [34, 39–46]. More recently, Type II IFPI sensor arrays, which have been demonstrated

to be low loss and highly multiplexable, have been utilized as chemical and temperature sensors. Through optimization of laser processing, the insertion loss of Type II IFPI devices has been optimized to be as low as 0.002 dB/device [35, 47].

It is highly desirable to have a fully distributed sensor to perform continuous measurements while harnessing high spatial resolution data for many industrial applications. Distributed fiber sensors based on optical frequency-domain reflectometry (OFDR) utilize the intrinsic Rayleigh scattering inside the fiber core and can sample physical parameter changes over a long distance with mm spatial resolution [48]. To extract the distributed sensing information, the OFDR algorithm performs a cross-correlation calculation between an unmodified Rayleigh backscattering profile and the disturbed temperature profile over each length segment or the gauge length along an optical fiber, that is related to the spatial resolution of the fiber sensor. By determining the shift of the correlation peak, accurate temperature change can be determined. However, Rayleigh scattering is an undesirable mechanism for commercial optical fibers as it induces increased propagation loss in telecommunication applications. The signal-to-noise ratio (SNR) of Rayleigh-scattering-based distributed sensors is limited by low intrinsic Rayleigh scattering of unmodified optical fibers. This can be solved using an optical fiber with an enhanced Rayleigh scattering level. The enhanced Rayleigh backscattering signal can increase the SNR of the fiber sensor. While a smaller gauge length is needed to obtain a correlation peak with sufficient strength, the sensor spatial resolution is also improved. Specialty fibers, such as the high-scattering, nanoparticle-doped fiber, could produce up to a 45 dB increase of the Rayleigh backscattering signal from standard fibers [49]. However, the fiber sensor cost is significantly higher; and the high temperature performance of the fiber has not been well studied.

To address these challenges, laser manufacturing methods have been demonstrated to artificially introduce scattering

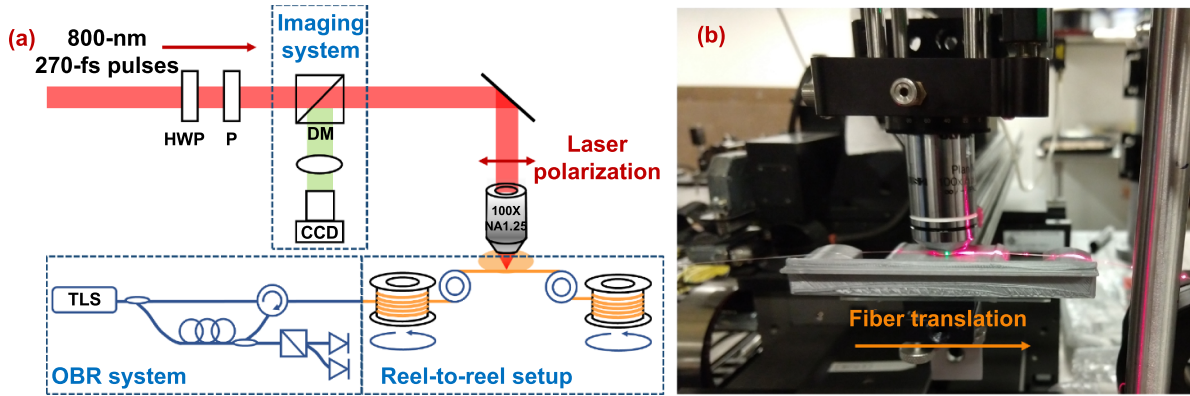


Figure 1. (a) The fabrication setup diagram. HWP: half-wave plate; P: polarizer; DM: dichroic mirror, TLS: tunable laser source. (b) A photo of the laser writing fabrication setup.

centers inside the low-cost commercial optical fibers to enhance the intrinsically low Rayleigh scattering signal for sensing applications. Both the UV laser [36, 50] and the femtosecond laser Type I modification [37, 51] were applied to a demodulation algorithm based on commercially available OFDR interrogators. Loranger *et al* demonstrated a UV-laser-induced, Rayleigh-enhanced section with up to a 50 dB return signal increase and an insertion loss of $0.0015 \text{ dB cm}^{-1}$ [36]. The method provided a temperature accuracy of $\sim 0.006^\circ\text{C}$ at a sensor gauge length of 1 cm on a single-mode fiber [50]. However, the method possesses limitations similar to those of UV FBGs, as the UV-laser-induced modifications are unstable for high temperature environmental applications. Femtosecond lasers have also been used to enhance standard optical fibers. Mihailov *et al* presented the results of a femtosecond-laser-induced Type I enhancement of 30 dB on a 10 cm fiber section with an insertion loss of $0.0008 \text{ dB cm}^{-1}$. The paper reported temperature performance from room temperature to 55°C with a standard deviation of 0.00085°C using a gauge length of 1 cm [37].

To improve the high-temperature resilience of laser-induced Rayleigh enhancement, Type II modification induced by femtosecond lasers has also been studied. A nanograting-based Rayleigh backscattering enhancement of $>40 \text{ dB}$ was demonstrated on a 17 cm long silica-core fiber that is stable up to 800°C . However, Type II modification incurs a higher propagation loss of $0.15\text{--}0.41 \text{ dB cm}^{-1}$ and limits the spatial scale of the distributed sensor [52]. More recently, this problem was addressed by engineering the nanograting morphology through fabrication procedure optimization. A Type II Rayleigh-enhanced signal of $>35 \text{ dB}$ was fabricated on a 3 m long standard telecom fiber (Corning SMF28e+) with an optimized loss of 0.01 dB cm^{-1} . The temperature stability at 1000°C was verified, while a temperature measurement accuracy of 0.012°C at room temperature was obtained using the gauge length of 1 cm [38].

In this paper, we provide a comprehensive discussion on femtosecond laser precision manufacturing techniques to

produce Type II nanograting in optical fiber cores for both multiplexable point and scattering-based distributed fiber sensor applications. Laser processing optimization to produce low-loss Type II devices is directly correlated to the formation and morphology of nanogratings inscribed inside fiber cores. High-temperature performance of both multiplexed IFPI point fiber sensors and distributed fiber sensors were studied from room temperature to 1000°C . To the best of our knowledge, we present the first demonstration of stabilized Type II sensors in nuclear reactors as validated by in-pile, lead-out testing of fiber sensors at 570°C in an operating research reactor with intense neutron flux of $\sim 1.2 \times 10^{14} \text{ fast neutron cm}^{-2} \text{ s}^{-1}$. Data presented in this paper shows that the low-cost telecommunication optical fiber can be hardened by femtosecond lasers to perform high spatial resolution measurements in extreme environments.

2. Fabrication, characterization, and optimization

2.1. Reel-to-reel fabrication of in-fiber sensors

The fabrication setup is schematically shown in figure 1(a). A Ti:sapphire regenerative femtosecond laser system was used. The laser delivered near-IR laser pulses of 800 nm wavelength at a fixed repetition rate of 250 kHz and a pulse duration of 270 fs. The pulse energy was controlled by a half-waveplate and a polarizer. The laser was linearly polarized at a direction perpendicular to the laser propagation direction and parallel to the fiber translation direction. Using a three-axis nanoprecision motion stage (Aerotech ABL20020) and an imaging system, the laser beam was focused inside the center of the fiber core. To mitigate the optical aberration induced by cylindrical geometry of the optical fiber shape, an oil-immersion objective (100 \times , NA 1.25) and index-matching oil ($n = 1.518$) were used to tightly focus the laser energy into the center of a fiber core, creating a modification area that was $2 \mu\text{m} \times 2 \mu\text{m}$ in cross-section and $3 \mu\text{m}$ in the axial direction.

A customized reel-to-reel laser fabrication setup was constructed for continuous fabrication of fiber sensors along an

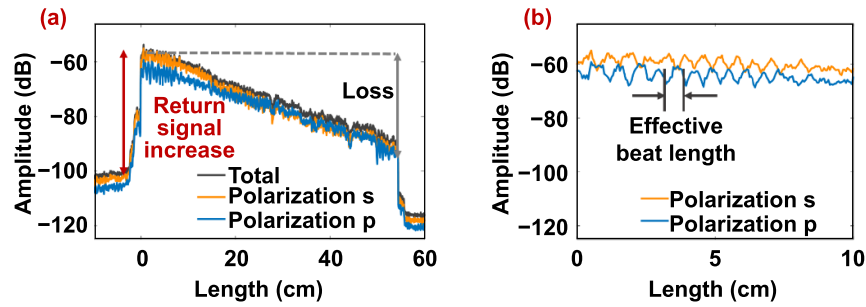


Figure 2. (a) The Rayleigh backscattering profile of a 55 cm long Rayleigh-enhanced distributed sensor section and (b) the enlarged profile of 0–10 cm of the sample, shown in (a).

optical fiber. It consisted of optical fiber reels, metal pulleys, fiber tension control structures, 3D printed fiber supporting structures, and a nanoprecision motion stage for the cross-sectional alignment. Figure 1(a) also shows a schematic of the commercially available Luna 4600 optical backscattering reflectometer (OBR) interrogator, which was used to monitor real-time Rayleigh backscattering profile modification of fiber under laser irradiation during the sensor fabrication. The OBR obtained a spatial-resolved Rayleigh backscattering signal based on an OFDR scheme. Light from a linearly swept tunable laser source (TLS) was split into a reference arm and a measurement arm, which included the fiber under test (FUT). The Rayleigh backscattered light from the FUT was then combined with the light from the reference arm to form a Mach–Zehnder interferometer. The interference between the Rayleigh backscattered light produced at a specific location on the FUT and light from the reference arm formed a fringe with a beat frequency directly related to the time delay between the two arms. The signals received by photodetectors contained interference signals from Rayleigh backscattered light along the entire FUT and were used to perform spatially resolved temperature and strain measurements.

Figure 1(b) is a photograph of the laser writing part of the reel-to-reel sensor fabrication system. The setup is able to fabricate both point and distributed fiber sensors through polymer coatings. Using the setup, optical fiber sensor devices can be continuously inscribed inside the optical fiber core, then monitored using the OBR for its characteristics, such as return signal increase and propagation loss. As presented in figure 2(a), the return signal increase of a distributed sensor can be extracted from an increase in the Rayleigh backscattering return signal in the modified region, as compared with the intrinsic Rayleigh scattering background of the unmodified fiber [53]. Meanwhile, the OBR can also be used to estimate the propagation loss of the sample from the Rayleigh profile slope [54, 55]. The OBR detects the Rayleigh backscattering signal using a polarization-diversity measurement. At the detector, the backscattering signal is split into two orthogonal polarizations by a polarization beam splitter. When light propagates through a birefringent fiber section, the group speed becomes different along the fast and slow axes. As the s- and p-polarizations of the OBR detector are not precisely aligned with the fast and slow axes of the sensing fiber, the light received at each detector channel has two components

of slightly different frequencies. The birefringence can be extracted from the OBR-measured polarization diverse signal. The polarizations are shown in figure 2(a) in orange and blue respectively, while the sum of the two polarizations is shown in black.

Figure 2(b) shows the enlarged first 10 cm section of the continuous sensor in figure 2(a), splitting into the s- and p-polarizations. The effective beat length l refers to the distance when light propagating along the fast and slow axis realizes a 2π phase shift. The birefringence can be calculated using $2\pi/l$. The detailed method used to calculate fiber birefringence using the OBR is presented in [38, 52, 56]. One limitation of this measurement method is that it cannot measure the birefringence over a longer distance, as demonstrated in figure 2(b), the beating fades away over the length of the measured region. While both the fast and slow modes propagate through the Rayleigh-enhanced region, their spatial difference becomes larger; and the coherence between the two polarization states fades when the spatial difference exceeds the resolution limit of the instrument. As a result, the polarization dependent behavior of the inscribed sensor inside an optical fiber can be extracted from the OBR.

2.2. Mechanisms

It has been reported that formation of nanograting in optical fibers induced by femtosecond laser irradiation contributes to high-temperature stabilities of femtosecond-inscribed FBG sensors [32, 33]. Previous microscopy studies demonstrated that nanograting is formed with periodical nanocracks that consist of nanopores of 10 s of nanometers in size, which is likely due to the silicon dioxide (SiO_2) decomposition caused by laser-induced electron plasma [57, 58]. Rayleigh scattering takes place due to inhomogeneities inside the fiber core with a feature size much smaller than the wavelength. The nanopores formed by laser irradiation provide additional scattering structures that generate stronger Rayleigh backscattering signals than those in unmodified fibers, which lead to improved SNR for fiber sensors [59]. Both Type II laser modifications and associated anisotropic scattering characteristics have been studied as a function of wavelength. Previous studies have demonstrated that Rayleigh scattering and Mie scattering can account for increased nanograting-induced scattering loss intensity [60–62].

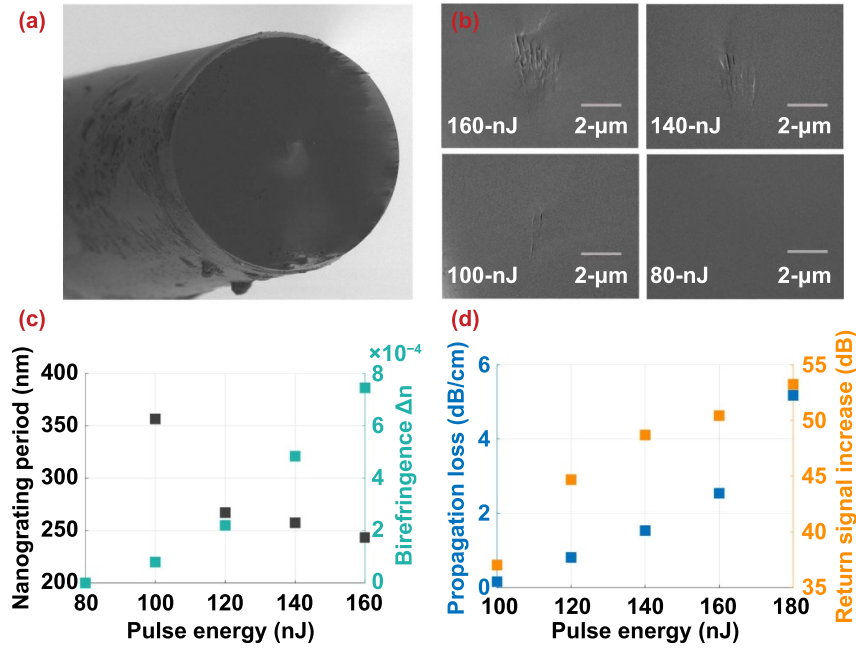


Figure 3. (a) A SEM photo of the optical fiber sensor cross-section with the nanograting in the core area, (b) the enlarged core area of nanograting sensors inscribed using different pulse energies, and (c), (d) the dependence of (c) the nanograting period (left) and birefringence (right) and (d) the propagation loss (left) and the SNR enhancement (right) of a Rayleigh-enhanced section on the fabrication laser pulse energy.

In this paper, a scanning electron microscope (SEM) was used to establish qualitative correlations between the morphology of nanogratings and insertion losses of fiber devices. Laser-irradiated fibers were cleaved at locations where Rayleigh profiles had been enhanced, which could be attributed to the formation of nanogratings inside the optical fiber core. Figures 3(a) and (b) present SEM photos of nanograting in the center of optical fiber cores. The threshold of nanograting formation is dependent on the fabrication conditions, including pulse energy and duration and laser repetition rate [63, 64]. For the results presented here, the formation of nanograting could be controlled by tuning the pulse energy, with the rest of the parameters fixed. Through SEM investigation of nanograting formation at different pulse energies (figure 3(b)), we found that nanogratings started to form when the laser pulse energy was over 100 nJ with a 270 fs pulse duration and a 250 kHz repetition rate. An increase in pulse energy led to an increase in the cross-sectional area where nanogratings were visible under SEM. Nanogratings were formed mostly within the laser focal volume, as demonstrated in the SEM photo shown in figure 3(b).

2.3. Characterization and optimization

Nanogratings inscribed by a linearly polarized femtosecond laser pulse are modulated nanostructures with a period much smaller than the wavelength. The modification area is comparable to a uniaxial negative crystal and is thus birefringent [65]. This characteristic can be used to characterize nanogratings through nondestructive methods using a crossed polarizer [66], a polarimeter [67], Bragg wavelength splitting [68], or the OBR [38, 52]. Using the OBR, the formation of the

birefringence was measured in real time during the laser fabrication process. A 5 cm Rayleigh-enhanced section was inscribed on an optical fiber sample at a fixed pulse energy and writing speed to measure the birefringence from the OBR. The fiber sample was then cleaved at the laser-modified section for SEM observation. The process was repeated for different pulse energies between 80 to 160 nJ.

Figure 3(c) summarizes the dependence of macroscale birefringence and microscale nanograting periodicity on laser pulse energy. Orientations of the nanograting visible in the SEM image were perpendicular to the fiber axial direction. However, when the laser pulse energy was reduced to 80 nJ, nanograting was not found by SEM studies, as shown in figures 3(b) and (c). No birefringence was measured by the OBR. This is consistent with the SEM photos. The Rayleigh enhancement at low pulse energy could be due to Type I laser modification [17, 18]. Even though transversal femtosecond writing methods are known to create an asymmetric refractive index profile for waveguide devices, the oil-immersion objective is known to produce laser modified regions with more symmetric cross-sections due to its high numerical aperture (NA) [22]. Thus, no birefringence formed in this regime. At a pulse energy larger than 100 nJ, nanograting began to form; and a beating signal could be measured by the OBR. As the pulse energy increased, the number of nanocracks and size of the nanograting also increased, while the period of the nanograting decreased. This led to an increase in the overall birefringence of the femtosecond-laser-modified region. With a pulse energy between 100 nJ and 160 nJ, a strong birefringence of up to 7.5×10^{-4} was generated, similar to that reported in previous literature [67, 68]. As such, the femtosecond-laser-fabricated, Rayleigh-enhanced fiber, due to

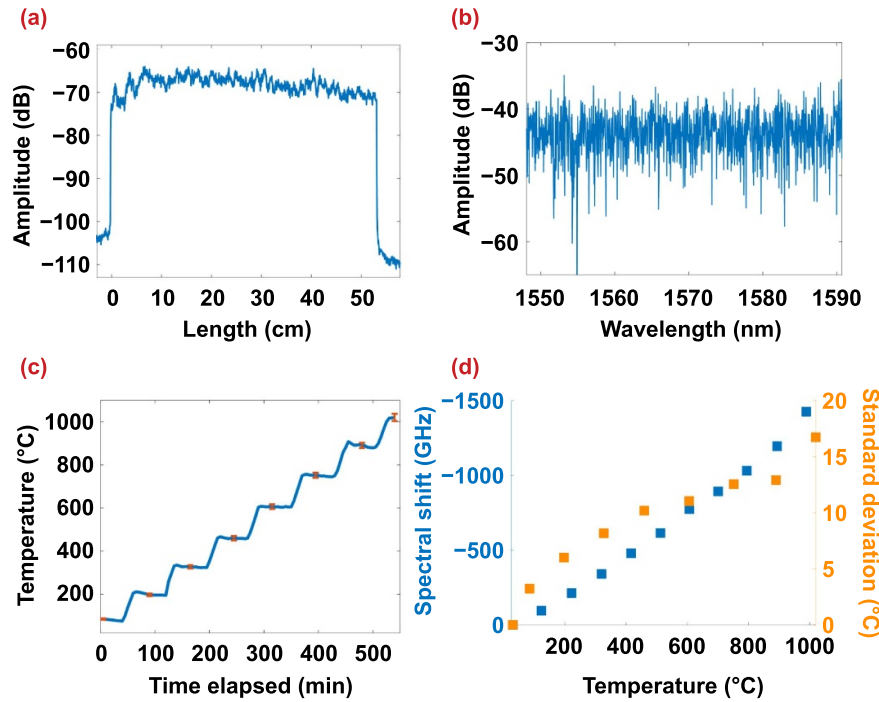


Figure 4. (a) The Rayleigh backscattering profile of a 53 cm Rayleigh-enhanced section inscribed on a single-mode optical fiber, (b) the spectrum of the reflected signal from the Rayleigh-enhanced section, (c) the temperature measurement extracted from the Rayleigh-enhanced section during one single heating cycle (the error bar shows the RMS variation across the Rayleigh-enhanced region), and (d) the spectral shift (left) and standard deviation (right) dependence on the environmental temperature change.

the high birefringence, can potentially be used for optical fiber polarization compensation devices or as multiparameter sensors.

Figure 3(d) explores these competing performance requirements for pulse energy values between 100 nJ and 180 nJ with Type II modification forms in the fiber core. In this range, a Rayleigh backscattering enhancement of 37 dB was achieved for a 100 nJ pulse energy. The scattering enhancement scaled almost linearly with pulse energy values between 100 nJ and 140 nJ from 37 dB to 49 dB. The laser-induced Rayleigh enhancement continued to increase in response to pulse energy values between 140 nJ and 180 nJ, which was far less significant than those occurring between 100 nJ and 140 nJ and from 49 dB to 53 dB. Propagation loss of a fiber sensor, measured by OBR, also increased linearly with the pulse energy between 100 nJ and 160 nJ and from 0.01 to 2.54 dB cm⁻¹. A significant increase in propagation loss was measured at 180 nJ at 5.17 dB cm⁻¹. It is known that optical scattering is the origin of the propagation loss in optical fibers. When nanograting is inscribed in fiber cores, the size and cross-sectional area of these artificial scattering structures in the fiber core can be qualitatively connected to the laser-induced propagation loss increase. This was confirmed by the combined SEM studies and optical measurements shown in figure 3. The gradual increase in nanograting areas found by SEM when the laser pulse energy was raised from 80 nJ to 160 nJ resulted in a monotonic increase of optical propagation loss measured by the OFDR, as shown in figure 3(d).

In summary, the combined optical and SEM studies of the laser writing conditions detailed in figure 3 shed light

on how to optimize the laser writing conditions to produce various types of fiber sensors, as the magnitude of the Rayleigh backscattering enhancement has to be balanced with the propagation loss. For example, to create an IFPI sensor for high-temperature applications, the fringe visibility could be a target for optimization, which is related to both the magnitude of the Rayleigh scattering enhancement and laser-induced propagation loss [35]. For distributed fiber sensors intended for the extreme radiation environment of nuclear reactors, strong Rayleigh enhancement might outweigh concerns on laser-induced propagation loss for sections of fibers that will be exposed to extreme neutron flux and subject to severe radiation-induced attenuation (RIA) [38]. By tuning the fabrication parameter of the laser pulse energy, sensors with optimized performance can be fabricated.

3. Temperature sensing performance

3.1. Rayleigh-enhanced fiber as distributed temperature sensors for high-temperature environments

High-temperature stable fiber sensors were fabricated using a femtosecond laser direct writing method by continuously translating the optical fiber along the axial direction using the reel-to-reel setup. Nanograting was continuously inscribed inside the optical fiber core. A 53 cm Rayleigh-enhanced section with a profile, shown in figure 4(a), was fabricated with an average increase in reflectivity of over 35 dB. A random distribution of broad frequencies in the IR range was observed at the backscattered signal from the Rayleigh-enhanced section

(figure 4(b)). The spectrum was akin to a number of random FBGs inscribed. When a temperature change occurred, a spectral shift took place at each location. Similar to an FBG sensor, the spectral shift was proportional to the temperature change. By performing a cross-correlation calculation between the spectrums of the measured FUT and that of the unmodified FUT for each gauge length, a distributed sensing measurement was obtained.

The sensor was first annealed at 1000 °C, followed by repeated heating and cooling cycles. During each cycle, the furnace temperature was raised at a ramp rate of 5 °C min⁻¹, kept stable at each step of 100 °C until 1000 °C was reached, then cooled down to room temperature. The temperature change was also tracked by a thermocouple for reference. The Rayleigh backscattering profile was recorded using an OBR system every 10 min. Figure 4(c) shows the optical fiber sensing temperature measurement from the third cycle. The linear fit coefficient was obtained from the first heating cycle to extract temperature information from the spectral shift measured by the OBR. The curve characteristics and standard deviation are shown in figure 4(d). The coefficient was found to be -0.66 °C GHz⁻¹. The standard deviation over the 53 cm Rayleigh-enhanced distributed sensor was found to be 0.01 °C at room temperature and 16.74 °C at a temperature of 1019 °C using a gauge length of 2 cm. The long-term stability such that the spectral shift quality of a Rayleigh-enhanced section remained robust above 0.8, even after 16 h under the high temperature of 1000 °C, was also studied [38]. This is above the threshold of spectral shift quality of the OBR suitable for valid temperature measurements [69]. Spectral shift quality of the unmodified section of the fiber, at the same time, degraded to less than 0.1 due to long-term exposure at high temperatures, probably as a result of the degradation of the intrinsic Rayleigh scattering in the fiber [38].

3.2. Multiplexed FBGs and IFPIs as high-temperature sensors

Using the femtosecond laser direct writing scheme, IFPIs can be fabricated inside a single-mode optical fiber core. The sensor was characterized using the interrogation setup, as shown in figure 5(a). The sensor interrogation setup consisted of a broadband source in the mid-IR range, a spectrometer, and a signal processing unit. Figure 5(b) shows an optical microscope image of a standard optical fiber with two laser-induced Rayleigh scattering reflectors separated by 287.7 μm. When an Er-doped fiber amplified spontaneous emission (ASE) broadband source with a center wavelength around 1550 nm was launched into the fiber, the laser-induced two Type II modification points produced light scattering that was clearly visible using an indium gallium arsenide (InGaAs) charge-coupled device (CCD) camera, as shown in figure 5(c). As a comparison, second-order Type II FBGs, 4.5 mm in length, were fabricated using the identical point-by-point inscription method. The same pulse energy of 100 nJ was used for inscription. A similar setup was used for the FBG interrogation shown in figure 5(d). The microscopic image and the near IR red light scattering behavior are also observed in figures 5(e) and

(f). These images provide visual evidence that Type II IFPI sensors (figure 5(c)) can incur significantly less insertion loss as compared to Type II FBG devices (figure 5(f)), as the Type II FBGs are made of thousands of laser-modified points.

Figure 5(g) shows a reflection spectrum from a single IFPI device. The laser-induced Type II scattering produced ~50 dB of backscattering enhancement as compared to the intrinsic in-fiber Rayleigh scattering, which amounts to ~0.001% of reflectance per scattering point. However, this was sufficient to produce strong interference fringes, as presented in figure 5(g). Figure 5(h) shows the nonzero-padded fast Fourier transform (FFT) spectrum of a single IFPI sensor inscribed on a single-mode fiber. The peak is highly distinguishable. Figure 5(i) shows interference fringes from 20 IFPI sensors multiplexed onto a single fiber. The cavities lengths of 20 IFPI sensors were determined from the FFT spectrum, as shown in figure 5(j) with their respective peaks marked by arrows. In addition to the laser pulse energy, the quality control of the IFPI sensor fabrication appeared to be very sensitive on areas where nanograting is inscribed inside the fiber core. This increases the manufacturing challenges to producing IFPI sensor arrays with consistent reflection peaks, as presented in figure 5(j). However, as long as the sensors are made from nanograting and the peaks in the FFT spectrum have a reasonable SNR, the measurements from the fiber sensor can be used for extreme environmental applications.

Figure 5(k) shows the spectrum of a single FBG sensor with the Bragg wavelength centered at 1546.9 nm. By inscribing FBGs with different Bragg wavelengths, six FBGs were multiplexed on the same fiber; the spectrum is shown in figure 5(l). The FBGs with a shorter Bragg wavelength were placed closer to the interrogation unit. It was observed that the Bragg wavelength peak magnitude of the multiplexed FBGs decreased with the multiplexation order, which was a result of the reduced transmitted light due to out-of-band loss. The FBG insertion loss fabricated here was measured to be ~0.21 dB per sensor. The number is much larger compared to the 0.002 dB per IFPI sensor, as we presented in a previous work [35].

Both IFPI and FBG can be interrogated using identical instruments, such as a broadband source and a CCD spectrometer, shown in figures 5(a) and (d). Using these instruments, we compared how IFPI and FBG are demodulated. For an FBG sensor, the spectrometer performed direct measurements and tracked the FBG wavelength shift. The hardware resolution of the FBG peak measurement was determined by the spectrometer, which had 512 pixels to cover a wavelength range from 1510 to 1590 nm or 156 pm/pixel. This is equivalent to 11.39 °C/pixel resolution, as the temperature coefficient for an FBG in a germania-doped, silica core fiber is 13.7 pm °C⁻¹ [70]. However, with additional information on the shape of FBG peaks, a number of algorithms can drastically improve the temperature measurement accuracy to 0.005 °C [71]. For a temperature change from a room temperature of 20 °C to 900 °C, the FBG peak will move more than 80 pixels.

In contrast, the IFPI spectrum (e.g. figure 5(g)) acquired by the CCD spectrometer cannot be used to directly measure the optical path difference Δl_{OPD} . FFT was used to reveal the cavity lengths of the IFPIs (e.g. figure 5(h)). The IFPI

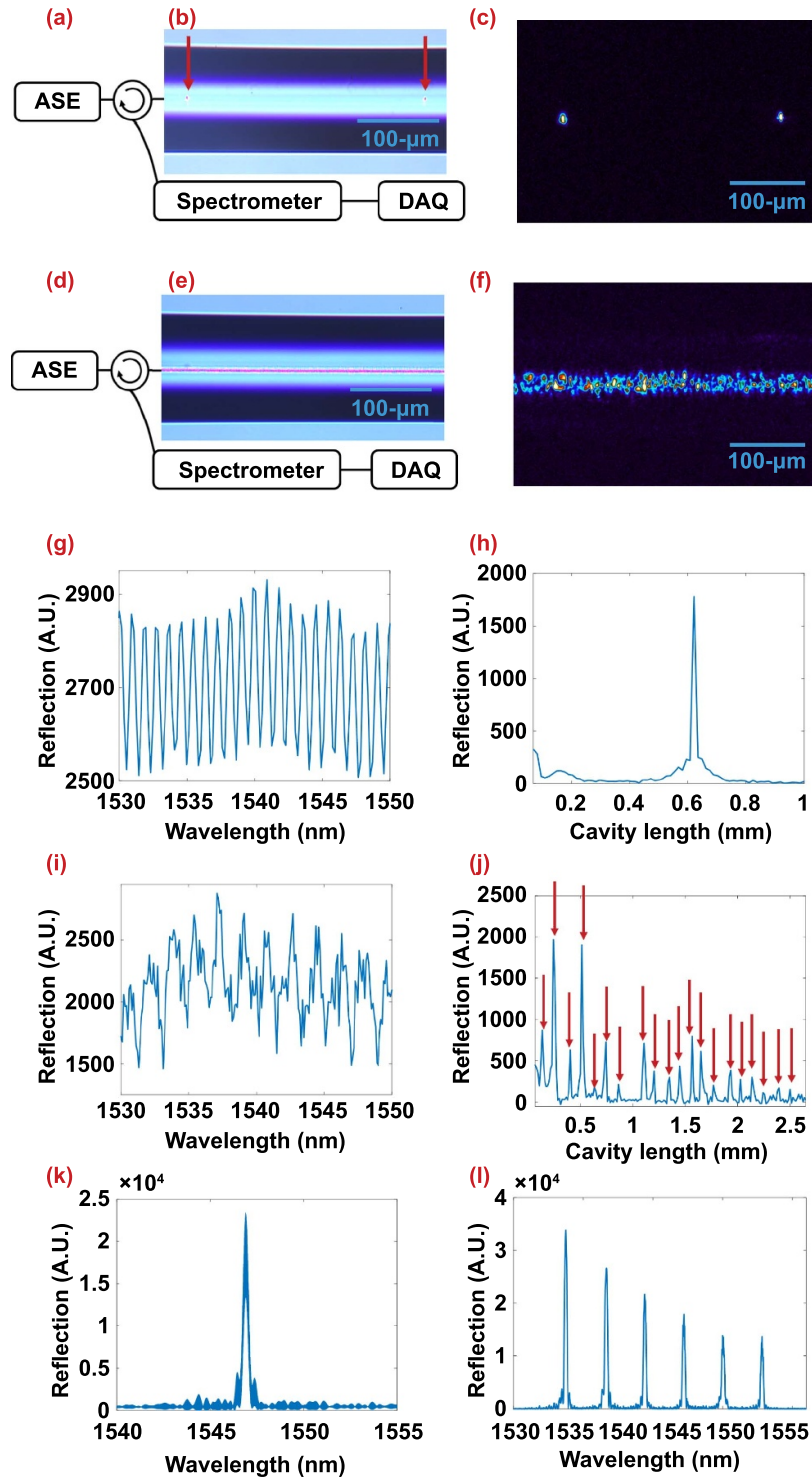


Figure 5. (a) The demodulation setup for the IFPIs. ASE: amplified spontaneous emission, DAQ: data acquisition unit, (b) the microscopic photo of the IFPI top view showing the nanograting reflectors scattering 638 nm red light, (c) the top view of the IFPI reflectors scattering 1550 nm light, (d) the demodulation setup for the FBGs, (e) the microscopic photo of the FBG top view with the 638 nm red light coupled to the fiber, (f) the top view of the FBG sensor scattering 1550 nm light, (g), (h) the fringe (g) and the FFT spectrum (h) of a femtosecond-laser-inscribed single IFPI with the cavity length of 620 μm, (i), (j) the fringe (i) and the FFT spectrum (j) of 20 multiplexed IFPIs, the peaks of the IFPI sensors are marked by red arrows, and (k), (l) the reflection spectrums of a single FBG (k) and six multiplexed FBGs (l).

cavity length resolution was also limited by the CCD spectrometer and bandwidth of the light source. If the interference spectrums of IFPI sensors were acquired from $\lambda_1 = 1510$ nm

to $\lambda_2 = 1590$ nm, the optical path difference Δl_{OPD} between two adjacent points in the FFT spectrum can be calculated by $\Delta \xi = 2\pi / (2\pi / \lambda_1 - 2\pi / \lambda_2)$ to be 30.1 μm. This means a

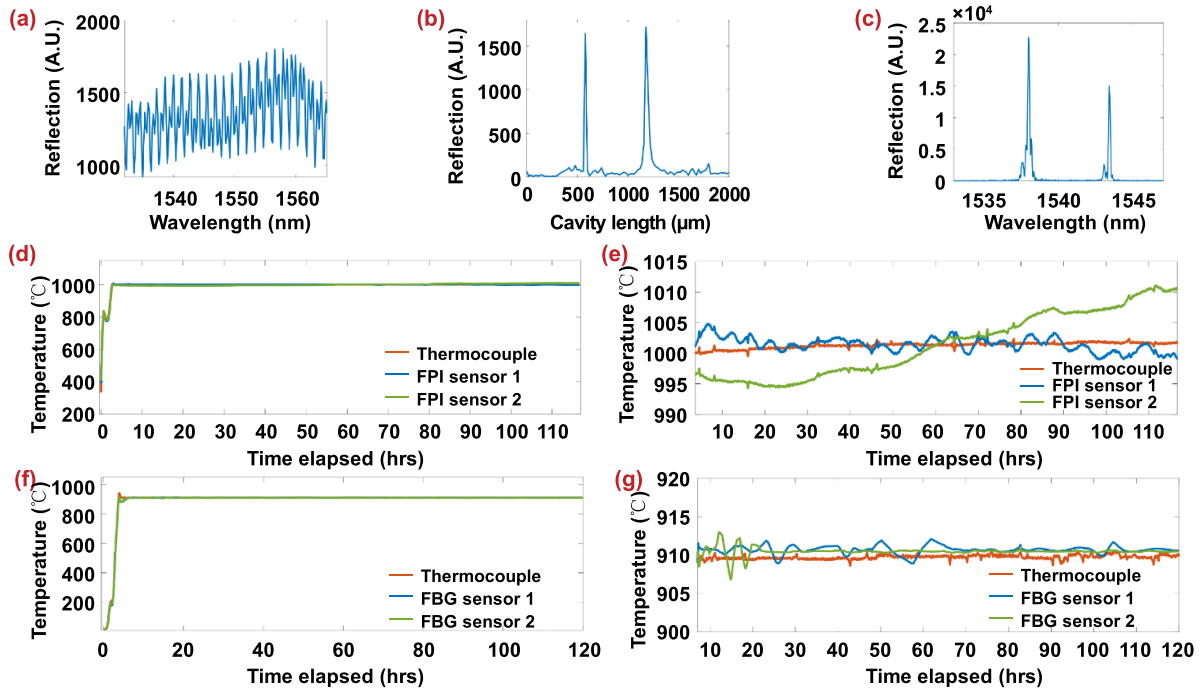


Figure 6. (a) The interference fringe of two multiplexed FPI sensors of 581.17 and 1191.61 μm cavity lengths, (b) the FFT spectrum of the fringe, (c) the reflection spectrum of two multiplexed FBG sensors, (d) the temperature measurement profile of the multiplexed IFPI sensors for five consecutive days, (e) the enlarged profile of (d) showing the temperature measurement fluctuation at 1000 $^{\circ}\text{C}$, (f) the temperature measurement profile of the multiplexed FBG sensors for five consecutive days, and (g) the enlarged profile of (f).

temperature rise from room temperature to 900 $^{\circ}\text{C}$ did not move an IFPI sensor with a cavity length of 1191.61 μm for even 1 pixel in its FFT spectrum. The accurate demodulation of ΔI_{OPD} relied on the phase information extracted from the FFT spectrum. Our previous publication presented a measurement accuracy of 0.007 $^{\circ}\text{C}$ for an IFPI with a 934.9 μm cavity length [35]. Peak widths of IFPI sensors in the FFT spectrum, as shown in figures 5(h) and (j), were determined by the interference spectrums. For the spectrometer used in this work, the 80 nm wavelength range yielded a theoretical limit on the peak width in the FFT spectrum of 36.31 μm (full width at half maximum). This set the minimal theoretical separation between the cavity lengths of the IFPI sensors that are to be multiplexed on a single fiber. In addition, the minimal spectral resolution of the CCD spectrometer (156 pm/pixel) determined the longest cavity length that can be demodulated. Using these two parameters, we can determine the maximum number of IFPI sensors multiplexable on a single fiber.

The long-term, high-temperature stability of the femtosecond-laser-inscribed IFPIs was tested at 1000 $^{\circ}\text{C}$. Two IFPI sensors were multiplexed onto a single-mode optical fiber (Corning SMF28e+) with cavity lengths of 581.17 and 1191.61 μm , respectively. A fast white-light interferometry demodulation scheme was used to demodulate IFPI fiber sensors to determine the cavity length in real time with a maximum demodulation rate of up to 5 kHz [72]. During demodulation, an FFT was performed on the fringe obtained from the spectrometer. The cavity length of each IFPI was demodulated from two data points near the peak in the nonzero-padded FFT spectrum, using the

Buneman frequency estimation and arithmetic calculations. The algorithm was chosen because of its fast speed, especially when simultaneously demodulating multiple multiplexed IFPI sensors. A detailed discussion of this demodulation scheme can be found in [73, 74]. Figures 6(a) and (b) show the fringe and the FFT spectrum used to determine cavity lengths. As a comparative study, the measurement was also performed on two FBGs multiplexed on a single-mode optical fiber. The central wavelengths of the FBG sensors were 1537.2 and 1542.5 nm, respectively, as presented in figure 6(c). The FBGs were demodulated using a Buneman frequency estimation algorithm. The details of the demodulation method are discussed in [71].

The fiber sensors were placed inside a furnace for testing under the condition of high temperatures over a span of 5 d. The temperature was tracked using a thermocouple. The temperature of the furnace was first increased from room temperature to 1000 $^{\circ}\text{C}$ at a ramp rate of $\sim 5^{\circ}\text{C min}^{-1}$. The linear fit curves were obtained from this temperature increase process for calibration and then used to measure the signal received from the sensors. The sensitivities of the sensors were measured to be 6.23 and 13.51 nm/ $^{\circ}\text{C}$. The sensor was then placed at 1000 $^{\circ}\text{C}$ for five consecutive days, as presented in figure 6(d). The temperature variation is shown at better resolution in figure 6(e). Thermal fluctuation can be seen at 1000 $^{\circ}\text{C}$ for both IFPIs. The oscillation was probably a result of furnace proportional integral derivative control cycles. These measurement results also show that fiber sensors have a higher fluctuation than electronic thermocouples, which is likely due to the smaller thermal mass of the fiber sensors. Overall, the

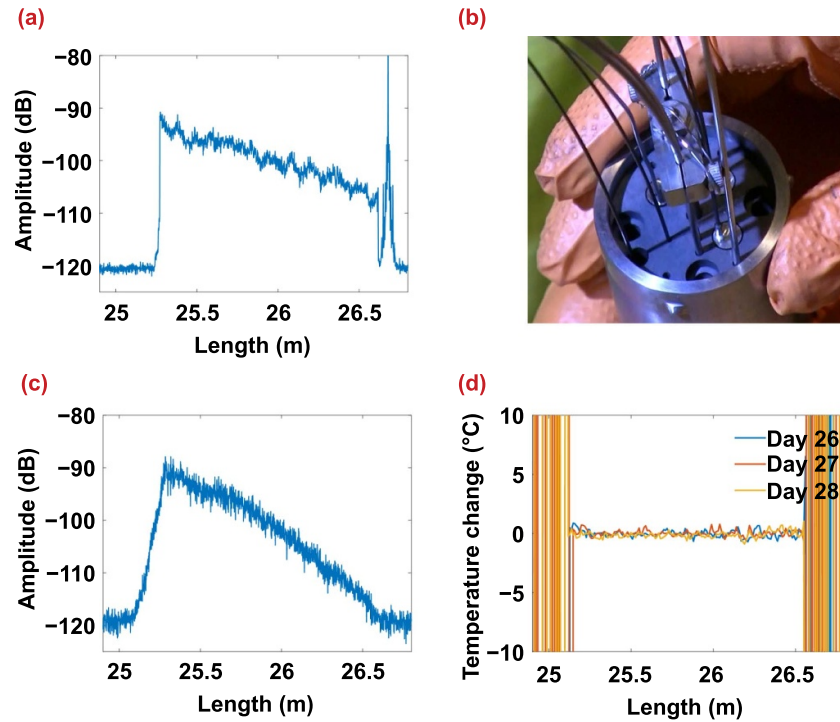


Figure 7. (a) The initial Rayleigh backscattering profile of a distributed fiber sensor with a 1.40 m Rayleigh-enhanced section (right), (b) photo of the fiber sensor holder capsule and the stainless steel tube containers, (c) the Rayleigh backscattering profile on the 28th day, and (d) the temperature measurement after 26–28 d of fast neutron radiation.

IFPI sensor with the cavity length of $581.17 \mu\text{m}$ showed a measurement fluctuation of 1.13°C . For the IFPI sensor with a cavity length of $1191.61 \mu\text{m}$, the measurement fluctuation was calculated to be 5.26°C . Another experiment was carried out for the two multiplexed FBG sensors up to a temperature of 910°C . The results are presented in figures 6(f) and (g). The sensitivities were measured to be 18.1 and $17.99 \text{ pm}/^\circ\text{C}$. Thermal fluctuations of 0.51°C and 0.52°C were measured for both sensors. A comparison using FBG sensor measurements exhibited a smaller temperature fluctuation. This was probably due to demodulation algorithms. Temperature changes measured by FBG sensors can be directly calculated from the FBG peak shifts. The IFPI cavity length changes were extracted from phase of FFT spectra, which are more susceptible to noise.

3.3. Rayleigh-enhanced fiber as high-temperature sensor under radiative environment

The core of an operating nuclear reactor is arguably the most extreme artificial environment. The safe operation of a nuclear power system can be greatly enhanced if high spatial resolution measurements inside a reactor core can be harnessed. At present, very limited information can be gathered inside a nuclear reactor core, as most sensors fail to withstand the harsh environment. In the last decade, optical fiber sensors have been considered for use in point measurements inside nuclear reactor cores [2–4]. In 2018, our group demonstrated that FBG fabricated on a silica core optical fiber using a femtosecond laser can withstand the extreme environment inside a

nuclear reactor core [29]. In this section, we show that the standard telecom fiber can be hardened using a femtosecond laser to execute distributed sensors under radiation. Using the femtosecond-laser-inscribed-nanogratings, the Rayleigh-enhanced backscattering profiles can lead to better SNR amid RIA to provide stable and high spatial resolution temperature measurements within a 1 cm spatial resolution.

Radiation resilience experiments on Rayleigh-scattering-based distributed optical fiber sensors using the femtosecond-laser-inscribed nanograting were carried out through collaboration with the Massachusetts Institute of Technology Nuclear Research Reactor (MITR). A 1.40 m Rayleigh-enhanced section was fabricated using a reel-to-reel oil-immersion setup on a Corning SMF28e+ single-mode optical fiber (figure 7(a)). This fiber was fabricated with 120 nJ pulse energy at a writing speed of 1 mm s^{-1} , which yielded a propagation loss of 0.09 dB cm^{-1} . The optical fiber samples were first inserted into a 316 stainless steel tube, which had an outer diameter of $1/16 \text{ in.}$ and a thickness of 0.01 in. The tube provided mechanical protection of the optical fiber samples but allowed fast neutrons to reach fiber samples with negligible attenuation [75]. The tubes were then installed into a capsule holder with electronic thermocouples to measure the reference temperature. Figure 7(b) shows a photo of the assembled capsule inserted into the nuclear reactor core. The fibers were irradiated in the MITR In-core Sample Assembly facility under fast neutron radiation. The irradiation temperature was maintained at a steady 560°C with a fast neutron flux at $\sim 1.2 \times 10^{14} \text{ ns}^{-1} \text{ cm}^{-2}$. Figure 7(c) presents the Rayleigh backscattering profile of the fiber samples in figure 7(a) after

28 consecutive days under radiation. The RIA, which can be gauged from the slope of the scattering profile, was estimated to be 0.21 dB cm^{-1} .

Figure 7(d) shows the temperature mapping of the in-core region on the 26th, 27th, and 28th day after the start of the fast neutron radiation. The unprocessed fiber section provided false measurements, which led to a measured temperature fluctuation $>1000^\circ\text{C}$. This was likely due to both small SNR of the intrinsic scattering and constant change of the Rayleigh scattering profile under irradiation. Meanwhile, the Rayleigh-enhanced section was still able to monitor the temperature, with a fluctuation smaller than 10°C at a gauge length of 5 cm. Overall, the nanograting-based femtosecond laser fabrication technique has significant potential to perform distributed measurements inside a reactor core to harness high spatial resolution data even using low-cost standard telecom fibers.

4. Conclusion

This paper presents a femtosecond laser manufacturing technique and shows the results in both distributed and multiplexable fiber sensors for use in high-temperature environmental conditions. Using a reel-to-reel laser direct writing scheme, nanograting was inscribed inside an optical fiber core. The performance of the fiber sensors was optimized by tuning the nanograting morphology. Long-term high temperature performance of the fiber sensors was tested at 1000°C . Sensor performance was also tested in extreme radiation environments in the MITR research reactor. The results presented in this paper show that it is feasible to fabricate both distributed and point fiber sensors using femtosecond lasers that can be utilized in applications with harsh environmental conditions. This method is able to harness high spatial resolution data, thus improving the safety and performance of engineering systems that operate in extreme environments.

Acknowledgments

This work was supported in part through Department of Energy Grants DE-NE0008686 and DE-FE00028992 and the NEET ASI program under DOE Idaho Operations Office Contract DE-AC07-05ID14517. The views and opinions of the authors expressed herein do not necessarily state or reflect those of the U.S. Government or any agency thereof.

ORCID iDs

Mohan Wang  <https://orcid.org/0000-0001-6678-4993>
 Yang Yang  <https://orcid.org/0000-0002-0671-7462>
 Sheng Huang  <https://orcid.org/0000-0001-9481-3579>
 Guiqiu Zheng  <https://orcid.org/0000-0002-5783-5848>
 Qingxu Yu  <https://orcid.org/0000-0003-0047-6220>
 Kevin P Chen  <https://orcid.org/0000-0003-1595-4475>

References

- [1] Calderoni P, Hurley D, Daw J, Fleming A and McCary K 2019 Innovative sensing technologies for nuclear instrumentation *2019 IEEE Int. Instrumentation and Measurement Technology Conf.* (Auckland: IEEE) pp 1–6
- [2] Chen H, Buric M, Ohodnicki P R, Nakano J, Liu B and Chorpene B T 2018 Review and perspective: sapphire optical fiber cladding development for harsh environment sensing *Appl. Phys. Rev.* **5** 011102
- [3] Mihailov S J 2012 Fiber Bragg grating sensors for harsh environments *Sensors* **12** 1898–918
- [4] Mihailov S J, Grobnc D, Hnatovsky C, Walker R B, Lu P, Coulas D and Ding H 2017 Extreme environment sensing using femtosecond laser-inscribed fiber Bragg gratings *Sensors* **17** 2909
- [5] Wang Z, Shen F, Song L, Wang X and Wang A 2007 Multiplexed fiber Fabry–Pérot interferometer sensors based on ultrashort Bragg gratings *IEEE Photonics Technol. Lett.* **19** 622–4
- [6] Wang Y, Gong J, Dong B, Wang D, Shillig T J and Wang A 2012 A large serial time-division multiplexed fiber Bragg grating sensor network *J. Lightwave Technol.* **30** 2751–6
- [7] Martinez A, Khrushchev I Y and Bennion I 2005 Thermal properties of fibre Bragg gratings inscribed point-by-point by infrared femtosecond laser *Electron. Lett.* **41** 176–8
- [8] Osellame R, Hoekstra H J W M, Cerullo G and Pollnau M 2011 Femtosecond laser microstructuring: an enabling tool for optofluidic lab-on-chips *Laser Photonics Rev.* **5** 442–63
- [9] Schaffer C B, Brodeur A, García J F and Mazur E 2001 Micromachining bulk glass by use of femtosecond laser pulses with nanojoule energy *Opt. Lett.* **26** 93–95
- [10] Mihailov S J, Smelser C W, Lu P, Walker R B, Grobnc D, Ding H, Henderson G and Unruh J 2003 Fiber Bragg gratings made with a phase mask and 800-nm femtosecond radiation *Opt. Lett.* **28** 995–7
- [11] Grobnc D, Smelser C W, Mihailov S J, Walker R B and Lu P 2004 Fiber Bragg gratings with suppressed cladding modes made in SMF-28 with a femtosecond IR laser and a phase mask *IEEE Photonics Technol. Lett.* **16** 1864–6
- [12] Williams R J, Krämer R G, Nolte S and Withford M J 2013 Femtosecond direct-writing of low-loss fiber Bragg gratings using a continuous core-scanning technique *Opt. Lett.* **38** 1918–20
- [13] Lai Y, Zhou K, Sugden K and Bennion I 2007 Point-by-point inscription of first-order fiber Bragg grating for C-band applications *Opt. Express* **15** 18318–25
- [14] Lu P, Mihailov S J, Ding H M, Grobnc D, Walker R B, Coulas D, Hnatovsky C and Naumov A Y 2018 Plane-by-plane inscription of grating structures in optical fibers *J. Lightwave Technol.* **36** 926–31
- [15] Zhou K, Dubov M, Mou C, Zhang L, Mezentssev V K and Bennion I 2010 Line-by-line fiber Bragg grating made by femtosecond laser *IEEE Photonics Technol. Lett.* **22** 1190–2
- [16] Lai Y, Chen Y and Cheong M W O 2016 Low-loss, high reflectivity, first-order, pitch-by-pitch fiber Bragg grating fabrication in truly free-standing single-mode fiber *J. Phys.: Conf. Ser.* **679** 012055
- [17] Della V G, Osellame R and Laporta P 2009 Micromachining of photonic devices by femtosecond laser pulses *J. Opt. A: Pure Appl. Opt.* **11** 013001
- [18] Itoh K, Watanabe W, Nolte S and Schaffer C B 2006 Ultrafast processes for bulk modification of transparent materials *MRS Bull.* **31** 620–5
- [19] Szameit A and Nolte S 2010 Discrete optics in femtosecond-laser-written photonic structures *J. Phys. B: At. Mol. Opt. Phys.* **43** 163001

- [20] Ams M, Marshall G D and Withford M J 2006 Study of the influence of femtosecond laser polarisation on direct writing of waveguides *Opt. Express* **14** 13158–63
- [21] Sakakura M, Lei Y, Wang L, Yu Y and Kazansky P G 2020 Ultralow-loss geometric phase and polarization shaping by ultrafast laser writing in silica glass *Light Sci. Appl.* **9** 15
- [22] Haque M, Lee K K C, Ho S, Fernandes L A and Herman P R 2014 Chemical-assisted femtosecond laser writing of lab-in-fibers *Lab Chip* **14** 3817–29
- [23] Glezer E N and Mazur E 1997 Ultrafast-laser driven micro-explosions in transparent materials *Appl. Phys. Lett.* **71** 882–4
- [24] Thomas J, Voigtländer C, Becker R G, Richter D, Tünnermann A and Nolte S 2012 Femtosecond pulse written fiber gratings: a new avenue to integrated fiber technology *Laser Photonics Rev.* **6** 709–23
- [25] Grobncic D, Hnatovsky C and Mihailov S J 2017 Thermally stable type II FBGs written through polyimide coatings of silica-based optical fiber *IEEE Photonics Technol. Lett.* **29** 1780–3
- [26] Grobncic D, Hnatovsky C and Mihailov S J 2016 Low loss type II regenerative Bragg gratings made with ultrafast radiation *Opt. Express* **24** 28704–12
- [27] Grobncic D, Smelser C W, Mihailov S J and Walker R B 2006 Long-term thermal stability tests at 1000 °C of silica fibre Bragg gratings made with ultrafast laser radiation *Meas. Sci. Technol.* **17** 1009–13
- [28] Hnatovsky C, Grobncic D and Mihailov S J 2018 High-temperature stable π -phase-shifted fiber Bragg gratings inscribed using infrared femtosecond pulses and a phase mask *Opt. Express* **26** 23550–64
- [29] Zaghloul M A S et al 2018 Radiation resistant fiber Bragg grating in random air-line fibers for sensing applications in nuclear reactor cores *Opt. Express* **26** 11775–86
- [30] Wei S, Wang Y, Yao H, Cavillon M, Poumellec B, Peng G D and Lancry M 2020 Thermal stability of type II modifications by IR femtosecond laser in silica-based glasses *Sensors* **20** 762
- [31] Bricchi E and Kazansky P G 2006 Extraordinary stability of anisotropic femtosecond direct-written structures embedded in silica glass *Appl. Phys. Lett.* **88** 111119
- [32] Hnatovsky C, Grobncic D, Coulas D, Barnes M and Mihailov S J 2017 Self-organized nanostructure formation during femtosecond-laser inscription of fiber Bragg gratings *Opt. Lett.* **42** 399–402
- [33] Mihailov S J, Hnatovsky C and Grobncic D 2019 Novel type II Bragg grating structures in silica fibers using femtosecond lasers and phase masks *J. Lightwave Technol.* **37** 2549–56
- [34] Deng J, Wang D N and Zhang H 2019 Femtosecond laser inscribed multiple in-fiber reflection mirrors for high-temperature sensing *J. Lightwave Technol.* **37** 5537–41
- [35] Wang M et al 2020 Multiplexable high-temperature stable and low-loss intrinsic Fabry–Perot in-fiber sensors through nanograting engineering *Opt. Express* **28** 20225–35
- [36] Monet F, Loranger S, Lambin-Iezzi V, Drouin A, Kadoury S and The K R 2019 ROGUE: a novel, noise-generated random grating *Opt. Express* **27** 13895–909
- [37] Lu P, Mihailov S J, Coulas D, Ding H and Bao X 2019 Low-loss random fiber gratings made with an fs-IR laser for distributed fiber sensing *J. Lightwave Technol.* **37** 4697–702
- [38] Wang M, Zhao K, Huang S, Wu J, Lu P, Ohodnicki P R, Li M J, Mihailov S J and Chen K P 2020 Reel-to-reel fabrication of in-fiber low-loss and high-temperature stable Rayleigh scattering centers for distributed sensing *IEEE Sens. J.* **20** 11335–41
- [39] Chen Z, Yuan L, Hefferman G and Wei T 2015 Ultraweak intrinsic Fabry–Perot cavity array for distributed sensing *Opt. Lett.* **40** 320–3
- [40] Deng J and Wang D N 2019 Ultra-sensitive strain sensor based on femtosecond laser inscribed in-fiber reflection mirrors and Vernier effect *J. Lightwave Technol.* **37** 4935–9
- [41] Chen P C and Shu X W 2018 Refractive-index-modified-dot Fabry–Perot fiber probe fabricated by femtosecond laser for high-temperature sensing *Opt. Express* **26** 5292–9
- [42] Deng J and Wang D N 2019 Construction of cascaded Fabry–Perot interferometers by four in-fiber mirrors for high-temperature sensing *Opt. Lett.* **44** 1289–92
- [43] Cui X, Zhang H and Wang D N 2020 Parallel structured optical fiber in-line Fabry–Perot interferometers for high temperature sensing *Opt. Lett.* **45** 726–9
- [44] Wang Q, Zhang H and Wang D N 2019 Cascaded multiple Fabry–Perot interferometers fabricated in no-core fiber with a waveguide for high-temperature sensing *Opt. Lett.* **44** 5145–8
- [45] Paixão T, Araújo F and Antunes P 2019 Highly sensitive fiber optic temperature and strain sensor based on an intrinsic Fabry–Perot interferometer fabricated by a femtosecond laser *Opt. Lett.* **44** 4833–6
- [46] Wang W, Ding D, Chen N, Pang F and Wang T 2012 Quasi-distributed IFPI sensing system demultiplexed with FFT-based wavelength tracking method *IEEE Sens. J.* **12** 2875–80
- [47] Cao R, Yang Y, Wang M, Yi X, Wu J, Huang S and Chen K P 2020 Multiplexable intrinsic Fabry–Perot interferometric fiber sensors for multipoint hydrogen gas monitoring *Opt. Lett.* **45** 3163–6
- [48] Soller B J, Gifford D K, Wolfe M S and Froggatt M E 2005 High resolution optical frequency domain reflectometry for characterization of components and assemblies *Opt. Express* **13** 666–74
- [49] Beisenova A, Issatayeva A, Korganbayev S, Molardi C, Blanc W and Tosi D 2019 Simultaneous distributed sensing on multiple mgo-doped high scattering fibers by means of scattering-level multiplexing *J. Lightwave Technol.* **37** 3413–21
- [50] Loranger S, Parent F, Lambin-Iezzi V and Kashyap R 2016 Enhancement of Rayleigh scatter in optical fiber by simple UV treatment: an order of magnitude increase in distributed sensing sensitivity *Proc. SPIE* **9744** 97440E
- [51] Xu Y, Lu P, Gao S, Xiang D, Mihailov S and Bao X 2015 Optical fiber random grating-based multiparameter sensor *Opt. Lett.* **40** 5514–7
- [52] Yan A, Huang S, Li S, Chen R, Ohodnicki P, Buric M, Lee S, Li M J and Chen K P 2017 Distributed optical fiber sensors with ultrafast laser enhanced Rayleigh backscattering profiles for real-time monitoring of solid oxide fuel cell operations *Sci. Rep.* **7** 9360
- [53] Froggatt M and Moore J 1998 High-spatial-resolution distributed strain measurement in optical fiber with Rayleigh scatter *Appl. Opt.* **37** 1735–40
- [54] Bauters J F, Heck M J R, John D, Dai D X, Tien M C, Barton J S, Leinse A, Heideman R G, Blumenthal D J and Bowers J E 2011 Ultra-low-loss high-aspect-ratio Si₃N₄ waveguides *Opt. Express* **19** 3163–74
- [55] Huang S, Li M, Garner S M, Li M J and Chen K P 2015 Flexible photonic components in glass substrates *Opt. Express* **23** 22532–43
- [56] Froggatt M E, Gifford D K, Kreger S, Wolfe M and Soller B J 2006 Characterization of polarization-maintaining fiber using high-sensitivity optical-frequency-domain reflectometry *J. Lightwave Technol.* **24** 4149–54
- [57] Lancry M, Brisset F and Poumellec B 2010 In the heart of nanogratings made up during femtosecond laser irradiation *Bragg Gratings, Photosensitivity, and Poling in Glass Waveguides 2010 21–24 June 2010* (Karlsruhe: OSA) BWC3

- [58] Rudenko A, Colombier JP and Itina T E 2018 Nanopore-mediated ultrashort laser-induced formation and erasure of volume nanogratings in glass *Phys. Chem. Chem. Phys.* **20** 5887–99
- [59] Kazansky P G, Inouye H, Mitsuyu T, Miura K, Qiu J, Hirao K and Starrost F 1999 Anomalous anisotropic light scattering in Ge-doped silica glass *Phys. Rev. Lett.* **82** 2199–202
- [60] Eaton S M, Chen W, Zhang H, Iyer R, Li J, Ng M L, Ho S, Aitchison J S and Herman P R 2009 Spectral loss characterization of femtosecond laser written waveguides in glass with application to demultiplexing of 1300 and 1550 nm wavelengths *J. Lightwave Technol.* **27** 1079–85
- [61] Amorim V A, Maia J M, Viveiros D and Marques P V S 2019 Loss mechanisms of optical waveguides inscribed in fused silica by femtosecond laser direct writing *J. Lightwave Technol.* **37** 2240–5
- [62] Åslund M L, Jovanovic N, Grothoff N, Canning J, Marshall G D, Jackson S D, Fuerbach A and Withford M J 2008 Optical loss mechanisms in femtosecond laser-written point-by-point fibre Bragg gratings *Opt. Express* **16** 14248–54
- [63] Hnatovsky C, Taylor R S, Rajeev P P, Simova E, Bhardwaj V R, Rayner D M and Corkum P B 2005 Pulse duration dependence of femtosecond-laser-fabricated nanogratings in fused silica *Appl. Phys. Lett.* **87** 014104
- [64] Richter S, Heinrich M, Döring S, Tünnermann A and Nolte S 2011 Formation of femtosecond laser-induced nanogratings at high repetition rates *Appl. Phys. A* **104** 503–7
- [65] Taylor R, Hnatovsky C and Simova E 2008 Applications of femtosecond laser induced self-organized planar nanocracks inside fused silica glass *Laser Photonics Rev.* **2** 26–46
- [66] Lammers K, Ehrhardt M, Malendevych T, Xu X, Vetter C, Alberucci A, Szameit A and Nolte S 2019 Embedded nanograting-based waveplates for polarization control in integrated photonic circuits *Opt. Mater. Express* **9** 2560–72
- [67] Lu P, Grobnc D and Mihailov S J 2007 Characterization of the birefringence in fiber Bragg gratings fabricated with an ultrafast-infrared laser *J. Lightwave Technol.* **25** 779–86
- [68] Fernandes L A, Grenier J R, Herman P R, Aitchison J S and Marques P V S 2012 Stress induced birefringence tuning in femtosecond laser fabricated waveguides in fused silica *Opt. Express* **20** 24103–14
- [69] Lu P, Byerly K, Buric M, Zandhuis P, Sun C, Leary A, Beddingfield R, McHenry M E and Ohodnicki P R Jr 2017 Distributed fiber-optic sensor for real-time monitoring of energized transformer cores *Proc. SPIE* **10194** 101941S
- [70] Othonos A 1997 Fiber Bragg gratings *Rev. Sci. Instrum.* **68** 4309–41
- [71] Yang Y, Wu J, Wang M, Wang Q, Yu Q and Chen K P 2020 Fast demodulation of fiber Bragg grating wavelength from low-resolution spectral measurements using Buneman frequency estimation *J. Lightwave Technol.* **38** 5142–8
- [72] Yang Y, Wang E, Chen K, Yu Z and Yu Q 2019 Fiber-optic Fabry–Perot sensor for simultaneous measurement of tilt angle and vibration acceleration *IEEE Sens. J.* **19** 2162–9
- [73] Yu Z and Wang A 2015 Fast white light interferometry demodulation algorithm for low-finesse Fabry–Pérot sensors *IEEE Photonics Technol. Lett.* **27** 817–20
- [74] Yu Z and Wang A 2016 Fast demodulation algorithm for multiplexed low-finesse Fabry–Perot interferometers *J. Lightwave Technol.* **34** 1015–9
- [75] Yilmaz E, Baltas H, Kiris E, Ustabas İ, Cevik U and El-Khayatt A M 2011 Gamma ray and neutron shielding properties of some concrete materials *Ann. Nucl. Energy* **38** 2204–12